Electronically Driven Structural Distortions in Lithium Intercalates of the $n = 2$ Ruddlesden−Popper-Type Host $Y_2Ti_2O_5S_2$: Synthesis, Structure, and Properties of $Li_xY_2Ti_2O_5S_2$ (0 < x < 2)

Geoffrey Hyett, Oliver J. Rutt, Zoltán A. Gál, Sophie G. Denis,
Michael A. Hayward, and Simon J. Clarke*

*Contribution from the Inorganic Chemistry Laboratory, Department of Chemistry,
University of Oxford, South Parks Road, Oxford, OX1 3QR, U.K.*

Received August 5, 2003; E-mail: simon.clarke@chem.ox.ac.uk

Abstract: Lithium intercalation into the oxide slabs of the cation-deficient $n = 2$ Ruddlesden−Popper oxysulfide $Y_2Ti_2O_5S_2$ to produce $Li_xY_2Ti_2O_5S_2$ (0 < x < 2) is described. Neutron powder diffraction measurements reveal that at low levels of lithium intercalation into $Y_2Ti_2O_5S_2$, the tetragonal symmetry of the host is retained: $Li_{0.30(5)}Y_2Ti_2O_5S_2$, $I4/mmm$, a = 3.80002(2) Å, c = 22.6396(2) Å, Z = 2. The lithium ion occupies a site coordinated by four oxide ions in an approximately square planar geometry in the perovskite-like oxide slabs of the structure. At higher levels of lithium intercalation, the symmetry of the cell is lowered to orthorhombic: $Li_{0.99(5)}Y_2Ti_2O_5S_2$, $Immm$, a = 3.82697(3) Å, b = 3.91378(3) Å, c = 22.2718(2) Å, Z = 2, with ordering of Li^+ ions over two inequivalent sites. At still higher levels of lithium intercalation, tetragonal symmetry is regained: $Li_{1.52(5)}Y_2Ti_2O_5S_2$, $I4/mmm$, a = 3.91443(4) Å, c = 22.0669(3) Å, Z = 2. A phase gap exists close to the transition from the tetragonal to orthorhombic structures (0.6 < x < 0.8). The changes in symmetry of the system with electron count may be considered analogous to a cooperative electronically driven Jahn−Teller type distortion. Magnetic susceptibility and resistivity measurements are consistent with metallic properties for x > 1, and the two-phase region is identified as coincident with an insulator to metal transition.

Introduction

Intercalation is important in the modification of materials properties.[1,2] Reductive topotactic insertion of alkali metals into transition-metal oxides[3] and sulfides[4] has been explored extensively in the context of producing electrochromic devices and in battery technology.[5−7] Other classes of solid such as fullerenes,[8] nitrides,[9] oxyhalides,[10] and nitride halides have also been investigated as hosts for intercalation, and the lithium intercalates of the layered group 4 nitride halides β-ZrNCl[11] and β-HfNCl[12] and the fullerides of the heavier alkali metals,

such as K_3C_{60},[13] are superconductors. Layered oxides such as the numerous and technologically important Ruddlesden−Popper (R−P) phases $(A_{n+1}M_nX_{3n+1})$,[14] which consist of perovskite slabs n octahedra thick separated by so-called rock salt layers, accept nonredox intercalants to increase the separation of the slabs[15] or exfoliate them.[16] Some R−P phases, such as $Sr_3Ru_2O_7$,[17] undergo topotactic *oxidative* intercalation of fluorine into the rock salt layers. Oxysulfides are a still rare class of solid-state compound in which the different chemical requirements of the two anions often result in materials with layered structures. The properties of these compounds are expected to provide new opportunities in solid-state science, and recent interest has been kindled in the layered LnCuOS compounds,[18] which consist of alternate LnO fluorite and CuS antifluorite layers. The groups of Tremel[19] and Meerschaut[20] have reported independently the layered oxysulfides with general formula

(1) Murphy, D. W. *Advances in the Synthesis and Reactivity of Solids: A Research Annual*; JAI Press: Greenwich, CT, 1991; Vol. 1, p 237.
(2) Rouxel, J.; Tournoux, M. *Solid State Ionics* **1996**, *84*, 141.
(3) Chippindale, A. M.; Dickens, P. G.; Powell, A. V. *Prog. Solid State Chem.* **1994**, *21*, 133.
(4) Eichhorn, B. W. *Progress in Inorganic Chemistry*; Karlin, K. D., Ed.; Wiley: New York, 1994; Vol. 42.
(5) Bruce, P. G. *Chem. Commun.* **1997**, 1817.
(6) Murphy, D. W.; Sunshine, S. A.; Zahurak, S. M. *NATO Adv. Sci. Inst. Ser., Ser. B* **1987**, *172*, 173.
(7) Murphy, D. W. *NATO Adv. Sci. Inst. Ser., Ser. E* **1985**, *101*, 181.
(8) (a) Rosseinsky, M. J.; Murphy, D. W.; Ramirez, A. P.; Fleming, R. M.; Zhou, O. *Springer Ser. Solid-State Sci.* **1993**, *117*, 11. (b) Murphy, D. W.; Rosseinsky, M. J. *NATO Adv. Sci. Inst. Ser., Ser. B* **1993**, *305*, 73.
(9) Bowman, A.; Mason, P. V.; Gregory, D. H. *Chem. Commun.* **2001**, 1650.
(10) (a) Jacobson, A. J. In *Solid State Chemistry: Compounds*; Cheetham, A. K., Day, P., Eds.; Oxford University Press: New York, 1992; pp 182−233. (b) Halbert, T. R. *Intercalation Chem.* **1982**, 375−403.
(11) Yamanaka, S.; Kawaji, H.; Hotehama, K.; Ohashi, M. *Adv. Mater.* **1996**, *8*, 771.
(12) Yamanaka, S.; Hotehama, K.; Kawaji, H. *Nature* **1998**, *392*, 73.

(13) Hebard, A. F.; Rosseinsky, M. J.; Haddon, R. C.; Murphy, D. W.; Glarum, S. H.; Palstra, T. T. M.; Ramirez, A. P.; Kortan, A. R. *Nature* **1991**, *350*, 600.
(14) Ruddlesden, S. N.; Popper, P. *Acta Crystallogr.* **1958**, *11*, 541.
(15) Mohan Ram, R. A.; Clearfield, A. J. *Solid State Chem.* **1994**, *112*, 288.
(16) Schaak, R. E.; Mallouk, T. E. *Chem. Mater.* **2000**, *12*, 3429.
(17) Li, R. K.; Greaves, C. *Phys. Rev. B* **2000**, *62*, 3811.
(18) Ueda, K.; Takafuji, K.; Hosono, H. *J. Solid State Chem.* **2003**, *170*, 182.
(19) Goga, M.; Seshadri, R.; Ksenofontov, V.; Gütlich, P.; Tremel, W. *Chem. Commun.* **1999**, 979.
(20) Boyer, C.; Deudon, C.; Meerschaut, A. *C. R. Acad. Sci. Paris, Ser. II* **1999**, *2*, 93.

$Ln_2Ti_2O_5S_2$ ($Ln = Pr - Er$, Y). These compounds resemble the $n = 2$ R−P phases, but the 12-coordinate site in the perovskite-like slabs is vacant, and the ordering between oxide and sulfide results in the oxide ions being confined to the perovskite slabs, while the sulfide ions occupy the rock salt layers. These compounds contain a reducible transition-metal cation, and their structural features resemble those of the ReO_3 structure as well as those of layered transition-metal sulfides, both of which will accept reducing intercalants. We have recently demonstrated[21] that sodium may be inserted either into the 12-coordinate site in the perovskite-like oxide slab (under thermodynamic control), producing α-$Na_xY_2Ti_2O_5S_2$ ($0 < x \leq 1$), or into a tetrahedral site in the sulfide layer (under kinetic control), producing β-$NaY_2Ti_2O_5S_2$ (with no apparent range of compositions), which is to our knowledge the first example of reductive intercalation into the rock salt layers of a Ruddlesden−Popper-type phase. The two phases of formula $NaY_2Ti_2O_5S_2$ (Ti oxidation state of +3.5) are both black with dominant Pauli paramagnetism, and detailed investigations of the α-Na_xY_2-$Ti_2O_5S_2$ ($0 \leq x \leq 1.0$) intercalates[22] and the intercalates with alkali metals inserted into the sulfide layers[23] are reported elsewhere. Here we describe the effect on the crystal structures of the insertion of variable amounts of lithium into the vacant sites in the oxide slabs of $Y_2Ti_2O_5S_2$. Some initial measurements on lithium intercalates of $Nd_2Ti_2O_5S_2$ are reported, but the yttrium system is reported in detail as this is the only member[19] for which measurements of magnetic properties are not complicated by the presence of a paramagnetic lanthanide ion. The smaller size of lithium means that, unlike in the sodium case, there is no kinetic barrier to insertion into the perovskite blocks even well below room temperature, and this is always favored over insertion into the rock salt-type sulfide layers. Furthermore, the lithium ion is accommodated in a different site in the oxide layers to that occupied by the sodium ion in the analogous sodium intercalates,[21] and lithium intercalates $Li_xLn_2Ti_2O_5S_2$ for $0 < x \leq 1.85(5)$ (i.e., approaching full occupancy of the lithium sites ($x = 2$) and with Ti oxidation states approaching +3) are chemically accessible. The details of the structures of these intercalates are strongly dependent on electron count. This work is complementary to the many investigations of reduced titanium oxides including Ti_2O_3,[24] $LnTiO_3$ ($Ln = Ce - Lu$, Y),[25] $La_{1-x}Sr_xTiO_3$,[26] $NaTiO_2$,[27] and the superconducting spinel $LiTi_2O_4$,[28,29] which show the interplay between crystal structure, electronic structure, and temperature for reduced titanate systems in the proximity of the metal−insulator boundary.

Experimental Section

Synthesis. The Li intercalates are all extremely air-sensitive and oxidize in a matter of seconds when exposed to air. All manipulations of solids were therefore carried out in a Glovebox Technology argon-

(21) Denis, S. G.; Clarke, S. J. *Chem. Commun.* **2001**, 2356.
(22) Clarke, S. J.; Denis, S. G.; Rutt, O. J.; Hill, T. L.; Hayward, M. A.; Hyett, G.; Gál, Z. A. *Chem. Mater.* **2003**, *15*, 5065.
(23) Rutt, O. J.; Hill, T. L.; Gál, Z. A.; Hayward, M. A.; Clarke, S. J. *Inorg. Chem.* **2003**, *42*, 7906.
(24) Mott, N. F. *J. Phys.* **1981**, *42*, 277.
(25) Greedan, J. E. *J. Less-Common Met.* **1985**, *14*, 335.
(26) Hays, C. C.; Zhou, J.-S.; Markert, J. T.; Goodenough, J. B. *Phys. Rev. B* **1999**, *60*, 10367.
(27) Clarke, S. J.; Fowkes, A. J.; Harrison, A.; Ibberson, R. M.; Rosseinsky, M. J. *Chem. Mater.* **1998**, *10*, 372.
(28) Johnston, D. C.; Prakash, H.; Zachariasen, W. H.; Viswanathan, R. *Mater. Res. Bull.* **1973**, *8*, 777.
(29) Harrison, M. R.; Edwards, P. P.; Goodenough, J. B. *Philos. Mag. B* **1985**, *52*, 679.

filled recirculating drybox with a combined O_2 and H_2O content of less than 5 ppm. Orange $Y_2Ti_2O_5S_2$ and brown $Nd_2Ti_2O_5S_2$ were prepared on the 2−10 g scale by reacting stoichiometric quantities of Y_2O_3 or Nd_2O_3, TiO_2, and TiS_2 at 1100 °C in sealed silica tubes. The lanthanide oxides (Y_2O_3: Aldrich 99.99%; Nd_2O_3: ALFA 99.99%) were dried at 900 °C for 24 h in air and then removed to the drybox, TiO_2 (Aldrich 99.9+%) was dried at 250 °C in air, and TiS_2 was prepared by reacting Ti (ALFA 99.99%, dehydrided) with S (ALFA 99.9995%) at 600 °C for 3−4 days in evacuated silica tubes. (Caution: the temperature was raised from 400 to 600 °C over 24 h to avoid a buildup of sulfur pressure.) The starting materials were ground together thoroughly and loaded into silica tubes which had been baked at 900 °C under a vacuum of 2×10^{-2} mbar for several hours to remove adsorbed moisture. This prebaking step was important to avoid contamination of the oxysulfides with $Ln_2Ti_2O_7$ phases (especially in the case of $Y_2Ti_2O_5S_2$). The tubes were sealed under a vacuum of 2×10^{-2} mbar, and the brown or orange oxysulfides were obtained phase pure according to laboratory powder X-ray diffraction by heating the tubes at 1100 °C for 3−4 days. Lithium intercalation was carried out in three different ways using either lithium vapor or reducing solutions containing the Li^+ ion. First, 2−5 g of the oxysulfide powders were reacted with excess *n*-BuLi (Aldrich, 2.5 M in hexane; Li/Ti ratios of between 7:1 and 10:1) at between 20 and 50 °C for 1−60 days under a nitrogen atmosphere. The samples were filtered and washed three times with distillation-dried hexane and then dried under vacuum prior to storage in the drybox. In the second low-temperature approach, applied to $Y_2Ti_2O_5S_2$, excess lithium (Li/Ti ratios of between 1:1 and 10:1) was dissolved in 30−50 cm^3 of liquid ammonia (BOC 99.98% and dried over sodium) in one arm of a glass "H"-cell[30] (designed to withstand an internal pressure of up to 15 atm) and poured onto 0.5−3 g of $Y_2Ti_2O_5S_2$ located in the other arm. The solution was stirred overnight at −78 °C after which the powder had changed in color from orange to black. The unreacted metal−ammonia solution was separated from the solid by means of a porous glass filter separating the two arms of the "H"-cell, and the solid was washed by condensing the ammonia back onto the solid and repeating the filtration step until the liquid in contact with the solid product was colorless. The ammonia was then removed to another vessel, and the "H"-cell was evacuated to 2×10^{-2} mbar and removed to the drybox prior to extraction of the solid product. In some cases, this treatment was then repeated with fresh Li/NH_3 solution for several periods of 24 h. If temperatures around 0 °C (Caution: the glassware must be designed to withstand the vapor pressure of ammonia and the pressure of any evolved H_2) were used for the intercalation using Li/NH_3, the $Li_xY_2Ti_2O_5S_2$ material formed in the reaction was found to catalyze the decomposition of the solution to $LiNH_2$ and H_2 over a period of a few hours (indeed, decomposition of alkaline earth/ammonia solutions was rapid even at −78 °C, and this route cannot be used for intercalation of the alkaline earths). These samples prepared using "chimie douce" approaches were used for neutron powder diffraction investigations and are summarized in Table 1. Alternatively, lithium vapor was used as the reducing agent: up to 2 g of the oxysulfide powders were placed in nickel tubes (Ni 222 alloy, 99.9% pure, 10 cm long, 9-mm inner diameter, 0.5-mm wall thickness, and sealed at one end) and a smaller stainless steel tube (5-mm inner diameter, open at one end) containing some lithium pieces (Li/Ti ratios of between 2:1 and 10:1) was placed on top of the powder. This assembly was used so that the oxysulfide powder was in contact only with lithium vapor and not the liquid. The nickel tube was sealed by arc-welding under argon (purified using a Ti getter at 800 °C), and the whole was sealed in an evacuated silica jacket to avoid oxidation of the nickel at elevated temperatures. These tubes were placed upright in a muffle furnace and heated at 400−700 °C for periods of 1−6 weeks.

(30) Wayda, A. L.; Dye, J. L. *J. Chem. Educ.* **1985**, *62*, 356.

Table 1. Summary of Synthetic Methods Used To Obtain Materials Li$_x$Y$_2$Ti$_2$O$_5$S$_2$

x in Li$_x$Y$_2$Ti$_2$O$_5$S$_2$	synthetic method	Li/Ti mole ratio	T/°C	duration	structural analysis	color
0.30(5)	*n*-BuLi/hexane	7:1	20	24 hours	D2B	dark green
0.66(5)[a]	*n*-BuLi/hexane	10:1	20	7 days	POLARIS	dark green
0.75(5)[a]	*n*-BuLi/hexane	7:1	20	7 days	D2B	dark green/black
0.95(5)	*n*-BuLi/hexane	7:1	50	24 hours	D2B	black
0.99(5)	*n*-BuLi/hexane	10:1	25	7 days	POLARIS	black
1.14(5)	*n*-BuLi/hexane	7:1	50	7 days	D2B	black
1.30(5)	Li/NH$_{3(l)}$	2:1	−78	4 × 48 hours	[b]not measured	black
1.50(5)	*n*-BuLi/hexane	10:1	50	60 days	POLARIS	black
1.52(5)	Li/NH$_{3(l)}$	1:1	−78	24 hours	POLARIS	black
1.85(5)	Li/NH$_{3(l)}$	2:1	−78	3 × 24 hours	POLARIS	black

[a] Two-phase materials. [b] Orthorhombic lattice parameters derived from PXRD data.

Chemical Analysis. Analysis for lithium was carried out using a Thermo Elemental Atomscan 16 ICP analyzer. The lithium ions were leached out of the intercalates by shaking the materials with deionized water.

Diffraction Measurements. Powder X-ray diffraction (PXRD) measurements to assess phase purity and determine lattice parameters were carried out using a Siemens D5000 diffractometer operating in Debye−Scherrer geometry with Cu Kα_1 radiation selected using a Ge(111) monochromator. The samples were ground with amorphous boron (1:1 mass ratio) to limit sample absorption and sealed in 1-mm diameter glass capillaries. Powder neutron diffraction (PND) measurements were carried out using the diffractometer POLARIS at the ISIS Facility, Rutherford Appleton Laboratory, U.K., or the high-resolution diffractometer D2B at the Institut Laue-Langevin, Grenoble, France. On POLARIS, samples of between 2 and 5 g in mass were measured in the d-spacing range $0.4 < d < 8$ Å by means of three banks of detectors located at scattering angles 2θ of 35° (^{3}He tube detector), 90° (ZnS scintillator), and 145° (^{3}He tube detector, highest resolution bank: $\Delta d/d = 5 \times 10^{-3}$) for a total integrated proton current at the production target of approximately 500/m μAhr where m is the mass in grams of the sample. On D2B samples of between 4 and 5 g in mass were measured in the 2θ range 5−150° using neutrons of wavelength 1.595 Å selected using a 28-crystal Ge(335) monochromator ($0.83 < d < 18.3$ Å). The diffraction pattern was measured using 64 ^{3}He tube detectors spaced at intervals of 2.5° in 2θ, and the entire detector bank was moved over this interval in steps of 0.05°. Measurements were made over periods of 6−8 h. Low-temperature measurements on D2B or POLARIS were carried out at 2 or 5 K achieved using an ILL "orange" cryostat. One sample was additionally measured on POLARIS at up to 400 °C in a Rutherford-Appleton Laboratory-designed furnace (RAL F2) with a cylindrical vanadium heating element and an evacuated sample space. All samples for neutron diffraction measurements were contained in 10-mm diameter thin-walled vanadium cans, which were sealed in the drybox with indium gaskets (or with a soft copper gasket in the case of measurements above room temperature). Rietveld refinement against PND data was carried out using the GSAS suite of programs.[31] Refinement against POLARIS data was carried out using all three detector banks simultaneously.

Magnetic Susceptibility Measurements. Measurements were carried out using a Quantum Design MPMS2 SQUID magnetometer in the temperature range 5−320 K and at magnetic fields of up to 5 T. Material (30−120 mg) was loaded into predried (100 °C) gelatine capsules, which were sealed with superglue immediately after removal from the drybox, and then immediately loaded into the magnetometer to avoid degradation of the samples due to the permeability of the gelatine capsules. Measurements of the susceptibility were made by measuring the magnetic moment of the paramagnetic samples as a function of temperature at fields of either 3 and 4 T or 4 and 5 T and determining the gradient of moment against field in this region. This was necessary because measurements of sample moment against field

showed that the samples, which have small paramagnetic moments, usually contained minuscule amounts of ferromagnetic impurities (probably nickel), which saturated at fields above 1 T. Corrections were carried out for core diamagnetism using standard tables.[32]

Results and Discussion

Synthesis. The powdered samples turned from orange/brown to dark green after approximately 1 h of stirring with *n*-BuLi at room temperature and to black after several days (Table 1). When Li/NH$_3$ solution, a considerably stronger reducing agent than *n*-BuLi,[6] was used as the reductant the solid turned black after a few hours even at −78 °C. The PXRD patterns of samples of Li$_x$Y$_2$Ti$_2$O$_5$S$_2$ covering the range $0 < x < 1.85(5)$ (Table 1) obtained by these methods were all indexed on a unit cell very similar in dimensions to that of the starting materials, and the intensity distributions of the diffraction patterns were also similar, indicating that insertion of lithium is topotactic. Compounds with compositions Li$_x$Y$_2$Ti$_2$O$_5$S$_2$ with $0 < x < 0.6$ or $x > 1.5$ were indexed on a body-centered tetragonal cell while materials with intermediate compositions $0.7 < x < 1.3$ were indexed on a body-centered orthorhombic cell with $a_{orth} \approx b_{orth} \approx a_{tet}$, $c_{orth} \approx c_{tet}$. Compositions Li$_x$Y$_2$Ti$_2$O$_5$S$_2$ with $0 < x \leq 1.5$ were all achieved by reaction with *n*-BuLi in hexane: compositions may be controlled in this range by changing the reaction time and temperature as summarized in Table 1. Lithium intercalation using Li/NH$_3$ solution is much more rapid, and Li$_x$Y$_2$Ti$_2$O$_5$S$_2$ with $x = 1.5$ was achieved in only 24 h at −78 °C, in contrast to the 60 days at 50 °C required using *n*-BuLi. In the *n*-BuLi reactions, the reducing nature of the intercalate leads to side reactions producing LiH when the highest Li content ($x \approx 1.5$) materials obtainable by this method are synthesized. The more reducing Li/NH$_3$ solution enabled Li contents of up to $x = 1.85(5)$ to be achieved using three 24 h treatments of the solid at −78 °C with fresh Li/NH$_3$ solution and intermediate workup. However, the Li$_x$Y$_2$Ti$_2$O$_5$S$_2$ products with x approaching 2 catalyze the decomposition of the metastable Li/NH$_3$ solution to LiNH$_2$ and H$_2$. Considerable amounts of LiNH$_2$ were therefore obtained in addition to the highest Li content materials. LiNH$_2$ is only sparingly soluble in liquid ammonia and was not washed out during workup of the reaction. Subsequent washing of the sample with tetrahydrofuran which had been dried immediately prior to use by distillation over potassium metal enabled all the LiNH$_2$ to be removed (as judged by comparison of the measured Li content of the washed sample, with the expected value based on the measured lattice parameters) with no apparent deintercalation

(31) Larson, A.; von Dreele, R. B. *The General Structure Analysis System*; Los Alamos National Laboratory: Los Alamos, NM, 1985.

(32) *Magnetic properties of transition metal compounds*; Landolt-Bornstein New Series II/10, supplement 2; Springer-Verlag: Berlin, 1979.

Table 2. Results of Rietveld Refinements of the Structures of Single-Phase $Li_xY_2Ti_2O_5S_2$ Materials against Neutron Powder Diffraction Data Collected at ILL (instrument D2B) or ISIS (instrument POLARIS)

compound	$Li_{0.30(5)}Y_2Ti_2O_5S_2$	$Li_{0.99(5)}Y_2Ti_2O_5S_2$	$Li_{1.52(5)}Y_2Ti_2O_5S_2$	$Li_{1.85(5)}Y_2Ti_2O_5S_2{}^a$
instrument	D2B (1.595 Å)	POLARIS	POLARIS	POLARIS
T/K	298	298	298	298
space group	*I4/mmm*	*Immm*	*I4/mmm*	*I4/mmm*
a/Å	3.80002(2)	3.83189(3)	3.91831(3)	3.94260(8)
b/Å	a	3.91881(3)	a	a
c/Å	22.6396(2)	22.3007(2)	22.0652(3)	21.9578(9)
V/Å^3	326.919(5)	333.876(6)	338.770(8)	341.31(2)
variables	27	98	77	88
χ^2	2.448	2.261	0.716^b	0.909^c
wR_p	0.0515	0.0149	0.0151	0.0074
$R(F^2)$	0.0477	0.0161	0.0398	0.0856

^{a} Contains substantial amount of $LiNH_2$. ^{b} $\chi^2 < 1$ due to slight undercollection of data. ^{c} $\chi^2 < 1$ due to large incoherent background arising from $LiNH_2$ impurity.

of lithium from the oxysulfide phase (lattice parameters before and after washing were unchanged). The products of insertion of Li vapor at temperatures of 400−500 °C were similar to those obtained by the reaction with *n*-BuLi. At reaction temperatures of 600 °C and above, additional phases including $YTiO_3$ were present in the PXRD patterns. The soft route using *n*-BuLi allows much more control of the composition and allows for the synthesis of larger quantities of higher purity material than does the vapor intercalation route. Consequently, materials made by the soft routes were used for the structural and property measurements.

Structures. The refinements of the structures of the lithium intercalates of $Y_2Ti_2O_5S_2$ and $Nd_2Ti_2O_5S_2$ were carried out using the structures of the parent oxysulfides as starting models with lattice parameters for each intercalate derived from laboratory X-ray powder diffraction measurements. Analysis of the resulting Fourier difference map for a tetragonal compound of stoichiometry $Li_{1.38(4)}Nd_2Ti_2O_5S_2$ indicated that in contrast to the analogous sodium intercalates,[21,22] in which Na^+ is located in the center of the 12-coordinate sites in the oxide slabs, Li^+ was located in the center of the 4-coordinate, approximately square "windows" separating pairs of adjacent 12-coordinate vacancy sites. There are two such sites per 12-coordinate vacancy in $Ln_2Ti_2O_5S_2$, and thus the limiting stoichiometry for Li intercalation is $Li_2Ln_2Ti_2O_5S_2$ (Ti^{III}) which is almost achievable in the case of $Li_{1.85(5)}Y_2Ti_2O_5S_2$ using Li/NH_3 solution. Rietveld analysis of the structures of two orthorhombic compounds $Li_{0.95(5)}Y_2Ti_2O_5S_2$ and $Li_{1.14(5)}Y_2Ti_2O_5S_2$ using data collected on D2B was initially carried out assuming that the two now-inequivalent four-coordinate Li^+ sites were equally occupied. Refinement of the fractional occupancies of these two sites showed instead that only the smaller and squarer of the two sites is occupied by Li for compositions up to $Li_xY_2Ti_2O_5S_2$ with $x \approx 1$. The orthorhombic distortion at certain levels of Li intercalation (and, hence, electron count as discussed further below) therefore results in ordering of the Li^+ cations over the available sites. Once the location of Li in the tetragonal and orthorhombic phases had been determined, most of the refinements proceeded without incident. The very wide range of *d*-spacings available on POLARIS allowed for reliable refinement of anisotropic displacement ellipsoids for all atoms. Refinement of anisotropic ellipsoids for Li in $Li_{0.99(5)}Y_2Ti_2O_5S_2$ led to a decrease in the agreement factor χ^2 to 2.262 from a value of 2.598 in the case of isotropic Li ellipsoids. The displacement ellipsoids for Li in all these intercalates are extremely elongated toward the centers of the 12-coordinate
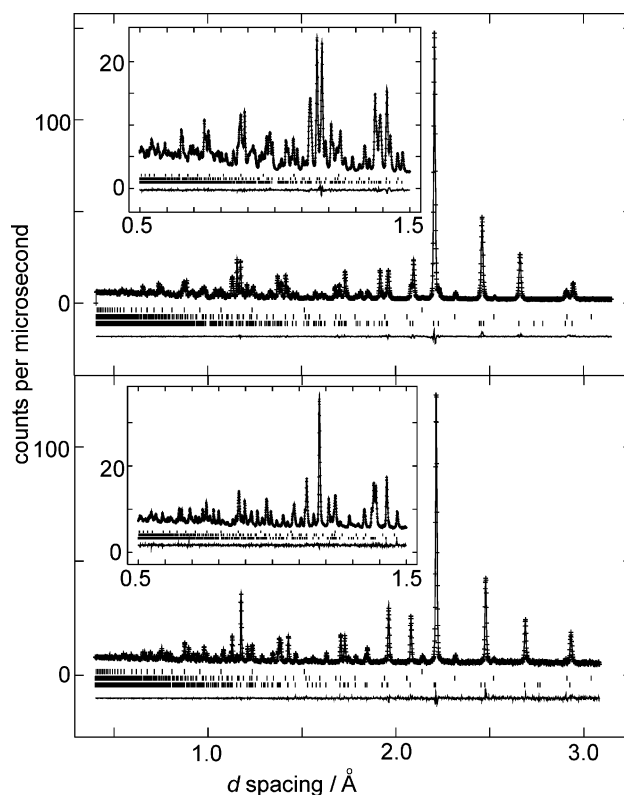

Figure 1. Results of Rietveld refinements of the structures of $Li_{0.99(5)}Y_2$-$Ti_2O_5S_2$ (top) and $Li_{1.52(5)}Y_2Ti_2O_5S_2$ (bottom) against POLARIS data (145° detector bank). The measured (points), calculated (line), and difference (lower line) profiles are shown. Tick marks indicate allowed reflections for the $Li_xY_2Ti_2O_5S_2$ phase (lower set), 1.7(1) mole % of a $Y_2Ti_2O_7$ impurity (middle set), and vanadium sample container (upper set). The insets show magnifications of the low *d*-spacing regions.

vacancy sites. This is suggestive of high Li^+ ion mobility in the solids, which is consistent with the much greater air sensitivity of these compounds when compared with the analogous sodium intercalates, from which the sodium ions may only be leached using dilute nitric acid solution.[21] The mobility of the lithium ions is under investigation. The refinement results for the range of compositions from $Li_{0.30(5)}Y_2Ti_2O_5S_2$ to $Li_{1.85(5)}Y_2Ti_2O_5S_2$ are presented in Table 2. Figure 1 compares the calculated and observed diffractograms following Rietveld refinement of the structures of $Li_{0.99(5)}Y_2Ti_2O_5S_2$ and $Li_{1.52(5)}Y_2$-$Ti_2O_5S_2$ at 295 K against POLARIS data. The compound $Li_{1.85(5)}Y_2Ti_2O_5S_2$, prepared using Li/NH_3 solution, contained a considerable amount of $LiNH_2$ (as discussed above), which was not noticeable in the X-ray diffraction pattern. This material
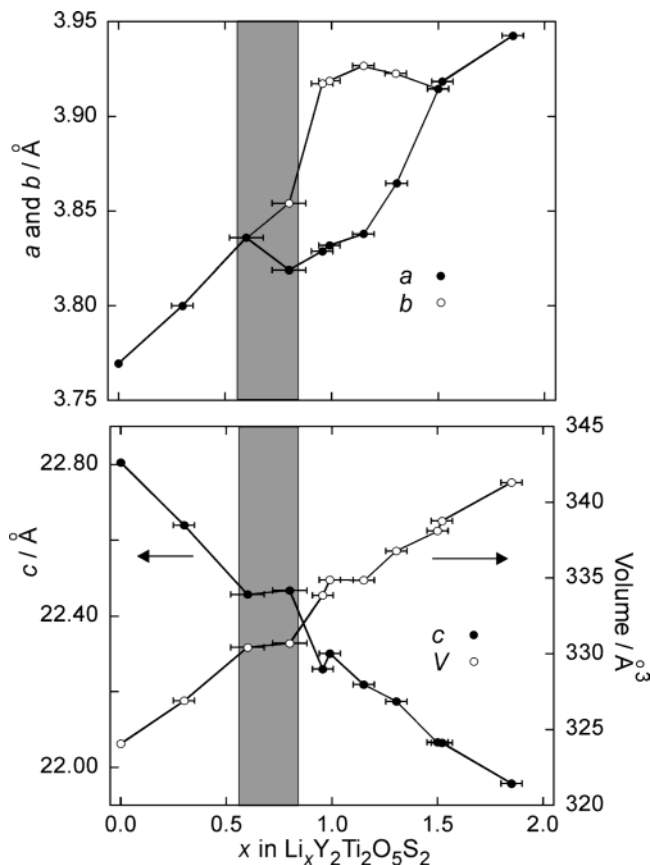
Figure 2. Lattice parameters and unit cell volume for $Li_xY_2Ti_2O_5S_2$ ($0 < x \leq 2$) as functions of x. a (●) and b (○) (upper) and c (●) and volume (○) (lower). The shaded area represents the two-phase region. The lines are guides to the eye.

was measured on POLARIS prior to washing with THF, and $LiNH_2$ was found to dominate the neutron diffraction pattern. In this case a two-phase (scattering fractions: $Li_2Y_2Ti_2O_5S_2$: 28%, $LiNH_2$: 72%) refinement using previously published structural data for $LiNH_2$[33] was satisfactory but did not permit stable refinement of anisotropic displacement ellipsoids for the atoms in $Li_{1.85(5)}Y_2Ti_2O_5S_2$. Li was assumed, following the results of refinements for the other compounds, to be the only significantly anisotropic atom in this phase, and its ellipsoid was fixed at the dimensions resulting from the refinement for $Li_{1.52(5)}Y_2Ti_2O_5S_2$. The cell parameters (($a + b$)/2 for the orthorhombic phases) vary approximately linearly with x as shown in Figure 2. Atomic parameters are presented in Table 3, and other structural data are described in detail below.

Materials with compositions around $Li_{0.7}Y_2Ti_2O_5S_2$, prepared using n-BuLi (stirred at 20 °C for 7 days), appeared to be orthorhombic when investigated by laboratory X-ray powder diffraction; however, refinements in the space group *Immm* of single orthorhombic phases for the sample of composition $Li_{0.75(5)}Y_2Ti_2O_5S_2$ (lattice parameters $a = 3.8186(1)$ Å, $b = 3.8758(1)$ Å, $c = 22.400(1)$ Å) against D2B data and for the sample of composition $Li_{0.66(5)}Y_2Ti_2O_5S_2$ (lattice parameters $a = 3.8194(1)$ Å, $b = 3.8608(1)$ Å, $c = 22.417(1)$ Å) against POLARIS data were unsatisfactory. Attempts to account for the data by lowering the symmetry to one of the monoclinic space groups *I2/m*, *C2/c*, *P2₁/n*, or the triclinic space group *I$\bar{1}$*

(33) Jacobs, H.; Juza, R. *Z. Anorg. Allg. Chem.* **1972**, *391*, 271.

or by using anisotropic strain broadening terms in the description of the profile function were all unsatisfactory. Annealing of the sample $Li_{0.66(5)}Y_2Ti_2O_5S_2$ at 380 °C for 4 days in a predried evacuated silica ampule produced a material which was apparently tetragonal according to laboratory X-ray powder diffraction with a c lattice parameter almost unchanged compared with the unannealed material and with an a parameter close to the mean of a and b in the apparently orthorhombic unannealed material. Investigation of the annealed sample of $Li_{0.66(5)}Y_2Ti_2O_5S_2$ on POLARIS showed that neither a single tetragonal phase in *I4/mmm* ($\chi^2 = 8.26$; $wR_p = 0.0370$) nor a single orthorhombic phase in *Immm* ($\chi^2 = 1.898$; $wR_p = 0.0177$) could adequately account for the data, but the data could be modeled satisfactorily, according to visual inspection and the numerical agreement factors, using approximately equal proportions of a tetragonal phase and an orthorhombic phase ($\chi^2 = 1.431$; $wR_p = 0.0153$). The two-phase refinement was carried out with anisotropic displacement ellipsoids for all atoms except Ti, with ellipsoid parameters of corresponding atoms in the two phases constrained as far as possible to be equal while respecting the different symmetries (a reasonable assumption based on the similarity of the two phases and required to enable refinement of the relative phase fractions), and with a similar constraint applied to peak profile parameters pertaining to the two lower-resolution data banks. All other structural parameters and the profile parameters for the more-discerning high-resolution ($2\theta = 145°$) data bank were independent for the two phases. The low scattering length of Li (-1.90 fm) relative to the other nuclei in the sample (Y = 7.75 fm, Ti = -3.30 fm, O = 5.805 fm, S = 2.847 fm), the intrinsically highly anisotropic nature of the Li ellipsoid, the various constraints applied, and correlations between refined parameters meant that although the Li contents of the two phases refined stably and reflected the overall Li content of the sample (although they were not constrained to do so), the Li content of the tetragonal phase was lower than expected (0.46(2)), and the Li content of the orthorhombic phase was higher than expected (1.04(4)) based on the lattice parameters and bond lengths of the two phases (see, for example, Figure 2). The refinement results for this two-phase refinement are shown in Figure 3 and Table 4. This two-phase behavior which was observed, although not investigated in detail, for $Li_xNd_2Ti_2O_5S_2$ phases of similar composition, is indicative of a composition gap between tetragonal materials and those which adopt the orthorhombic structure. When materials with compositions in the gap region are made at room temperature, they apparently consist of more than two phases: annealing results in the formation of one tetragonal phase and one Li-richer orthorhombic phase, but single-phase material within certain composition limits (see below) is apparently not stable with respect to disproportionation at room temperature. The structural parameters for the tetragonal and orthorhombic phases which are assumed to represent the edges of the phase gap region are presented in Table 5. The sample $Li_{0.66(5)}Y_2Ti_2O_5S_2$ was measured at elevated temperatures to determine whether a single phase with this composition was attainable via comproportionation. In the refinements against room temperature data, the tetragonal 200 and 204 reflections were particularly poorly accounted for using a single tetragonal phase. At 200 °C, the full widths at half-maximum of these reflections had 74% of their room temperature values, while the manifold of the most

Table 3. Atomic Parameters for Single-Phase Samples $Li_xY_2Ti_2O_5S_2$ Obtained from Refinement against Neutron Powder Diffraction Data

atom/site	refined parameter	$Y_2Ti_2O_5S_2{}^a$	$Li_{0.30(5)}Y_2Ti_2O_5S_2$	$Li_{0.99(5)}Y_2Ti_2O_5S_2$	$Li_{1.52(5)}Y_2Ti_2O_5S_2$	$Li_{1.85(5)}Y_2Ti_2O_5S_2$
		I4/mmm	*I4/mmm*	*Immm*	*I4/mmm*	*I4/mmm*
Y ($0\ 0\ z$)	z	0.333589(9)	0.33378(4)	0.33471(1)	0.33555(2)	0.33637(7)
	$100 \times (U_{iso,eq}/Å^2)$	0.53(1)	0.49(2)	0.59(1)	0.61(1)	0.45(2)
Ti ($0\ 0\ z$)	z	0.07867(2)	0.08035(8)	0.08458(2)	0.08758(4)	0.0888(1)
	$100 \times (U_{iso,eq}/Å^2)$	0.39(1)	0.35(8)	0.31(2)	0.36(2)	0.56(5)
O1a ($^1/_2\ 0\ z$)	z	0.099313(8)	0.09905(4)	0.10243(2)	0.09732(2)	0.09730(7)
	$100 \times (U_{iso,eq}/Å^2)$	0.57(1)	0.59(2)	0.64(1)	1.15(2)	1.33(3)
O1b ($0\ ^1/_2\ z$)	z			0.09366(2)		
	$100 \times (U_{iso,eq}/Å^2)$			0.76(2)		
O2 ($0\ 0\ 0$)	$100 \times (U_{iso,eq}/Å^2)$	1.05(1)	1.48(4)	0.78(2)	0.73(2)	0.85(6)
S ($0\ 0\ z$)	z	0.20469(2)	0.20448(9)	0.20472(3)	0.20484(5)	0.2032(2)
	$100 \times (U_{iso,eq}/Å^2)$	0.55(2)	0.36(5)	0.54(2)	0.48(3)	0.39(5)
Li ($0\ ^1/_2\ 0$)	$100 \times (U_{iso,eq}/Å^2)$		4.2(7)	4.16(2)	4.97(3)	4.97^c
	Li fraction^b		0.15^c	1.002(8)	0.78(1)	0.98(3)

^{a} From ref 21. ^{b} For tetragonal samples, x in $Li_xY_2Ti_2O_5S_2$ corresponds to double the fractional occupancy; for orthorhombic samples it is equal to the fractional occupancy. ^{c} Not refined.

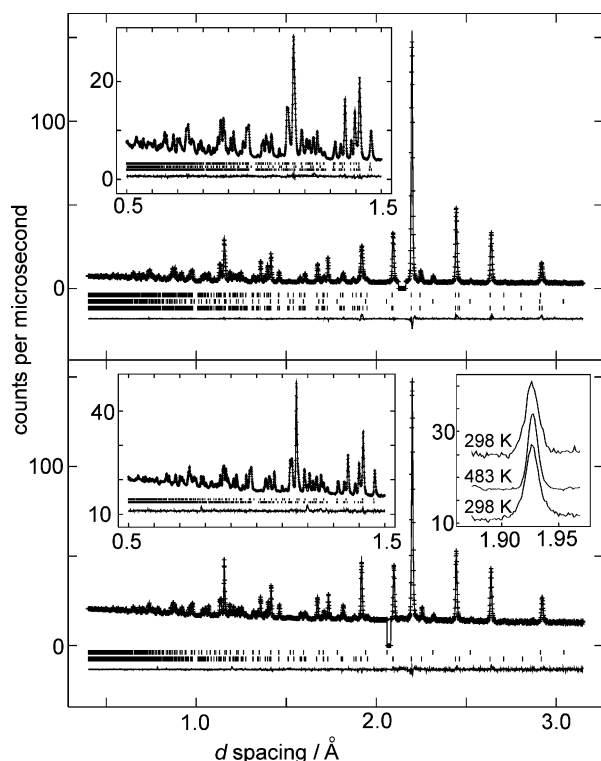***Figure 3.*** Results of Rietveld refinements of the sample with composition $Li_{0.66(5)}Y_2Ti_2O_5S_2$ against POLARIS data (145° detector bank). The measured (points), calculated (line), and difference (lower line) profiles are shown, and tick marks indicate allowed reflections. The upper diffraction pattern measured at 298 K was modeled using 42(1) % orthorhombic "$Li_{0.8}Y_2Ti_2O_5S_2$" (lowest set of tick marks), 58(1) % tetragonal "$Li_{0.6}Y_2Ti_2O_5S_2$" (uppermost set of tick marks), and 1.7(1) mole % of a $Y_2Ti_2O_7$ impurity (middle set of tick marks). The lower diffraction pattern, measured at 483 K, was modeled using a single tetragonal phase (lower set of tick marks) and the $Y_2Ti_2O_7$ impurity (upper set of tick marks). Peaks arising from the vanadium sample holder and furnace element were excluded. The left-hand insets show magnifications of the low *d*-spacing regions. The right-hand inset accompanying the high-temperature diffraction pattern shows, from top to bottom, the narrowing of the manifold arising from the 200/020 reflections on warming from 298 K (two-phase material) to 483 K (one-phase material) and the broadening which accompanies disproportionation on cooling back to 298 K.

intense and almost perfectly overlapping 116 reflections maintained its width on heating to 200 °C. Refinement of a single tetragonal phase in *I4/mmm* against data measured at 210 °C proceeded without incident, and agreement factors of $\chi^2 = 1.039$, $wR_p = 0.0092$, coupled with an excellent visual fit to the data

Table 4. Results of Rietveld Refinements of the Structures of Phases Constituting the Sample $Li_{0.66(5)}Y_2Ti_2O_5S_2$ against Neutron Powder Diffraction Data Collected on POLARIS at 298 K (sample is two phase) and at 483 K (sample is single phase)

compound	$Li_{0.66(5)}Y_2Ti_2O_5S_2$		$Li_{0.66(5)}Y_2Ti_2O_5S_2$
instrument	POLARIS		POLARIS
T/K	298		483
space group	*I4/mmm*	*Immm*	*I4/mmm*
phase fraction	0.58(1)	0.42(1)	1.0
a/Å	3.83590(5)	3.8189(2)	3.83378(4)
b/Å	*a*	3.8542(2)	*a*
c/Å	22.4566(5)	22.468(1)	22.5319(3)
V/Å^3	330.43(1)	330.70(2)	331.170(9)
variables	93		95
χ^2	1.431		1.039
wR_p	0.0153		0.0092
$R(F^2)$	0.0249		0.0664

confirmed that the material $Li_{0.66(5)}Y_2Ti_2O_5S_2$ was single phase above 200 °C. The results of this refinement are shown in Tables 4 and 5, and the fit is shown in Figure 3. After the sample was cooled to room temperature, the 200 and 204 reflections broadened, indicating disproportionation of the sample to the previously determined orthorhombic and tetragonal phases. Measurements of the diffraction pattern after further heating above 200 °C and further cooling to room temperature confirmed that the transformation was reversible (see inset to Figure 3).

The structures of the intercalates are shown in Figure 4, and the detail of the TiO_5S coordination polyhedron as a function of composition is shown in Figure 5. The relationship between structure and electron count will be discussed for the yttrium derivatives. The Ti−O, Ti−S, and Li−O bond lengths and the O−Ti−O bond angles for the full range of $Li_xY_2Ti_2O_5S_2$ intercalates, and including $Y_2Ti_2O_5S_2{}^{21}$ as the $x = 0$ member, are shown in Figures 6−8. In $Y_2Ti_2O_5S_2$, Ti is in approximately octahedral coordination by four "equatorial" O atoms (O1) at 1.9427(1) Å, one "apical" O atom (O2) at 1.7941(4) Å, and by an S atom at the opposite apex 2.8741(6) Å distant. The Ti−S distance is a long bonding distance in $Y_2Ti_2O_5S_2$, and Ti lies out of the plane described by the four equatorial O atoms and toward the apical O atom as shown in Figure 5. On intercalation of lithium, electrons enter bands which are Ti−O π-antibonding; all the Ti−O distances therefore increase as shown in Figure 6, and furthermore, the Ti atom moves toward the plane of the equatorial O atoms (Figure 5). Thus, the basal *a* lattice parameter (or the mean of *a* and *b* in the orthorhombic cases) increases

Table 5. Atomic Parameters for the Two Phases Used To Model the Neutron Powder Diffraction Pattern of Material with Composition $Li_{0.66(5)}Y_2Ti_2O_5S_2$ at 298 K and the Corresponding Parameters for the Single Phase Required at 483 K[a]

atom/site	parameter	"$Li_{0.6(1)}Y_2Ti_2O_5S_2$"	"$Li_{0.8(1)}Y_2Ti_2O_5S_2$"	$Li_{0.66(5)}Y_2Ti_2O_5S_2$
	T/K	298	298	483
	phase fraction	0.58(1)	0.42(1)	1.0
	space group	$I4/mmm$	$Immm$	$I4/mmm$
Y (0 0 z)	z	0.33459(6)	0.3337(1)	0.33413(2)
	$100 \times (U_{iso,eq}/Å^2)$	0.74(2)[b]	0.61(4)[b]	1.03(2)
Ti (0 0 z)	z	0.0826(1)	0.0824(2)	0.08215(4)
	$100 \times (U_{iso,eq}/Å^2)$	0.43(1)[b]	0.43(1)[b]	0.58(3)
O1a ($^1/_2$ 0 z)	z	0.09888(5)	0.1012(1)	0.09869(2)
	$100 \times (U_{iso,eq}/Å^2)$	0.98(2)[b]	0.98(2)[b]	1.33(2)
O1b (0 $^1/_2$ z)	z		0.0965(1)	
	$100 \times (U_{iso,eq}/Å^2)$		0.98(2)[b]	
O2 (0 0 0)	$100 \times (U_{iso,eq}/Å^2)$	1.14(4)[b]	1.09(8)[b]	2.12(3)
S (0 0 z)	z	0.2056(1)	0.2030(2)	0.20455(4)
	$100 \times (U_{iso,eq}/Å^2)$	0.47(4)[b]	0.61(4)[b]	0.83(4)
Li ($^1/_2$ 0 0)	$100 \times (U_{iso,eq}/Å^2)$	9.3(3)[b]	9.3(3)[b]	19(1)
	Li fraction	0.23(1)	1.04(4)	0.34(1)

[a] The compositions of the two phase sample are estimated to be $Li_{0.6(1)}Y_2Ti_2O_5S_2$ (tetragonal) and $Li_{0.8(1)}Y_2Ti_2O_5S_2$ (orthorhombic). [b] Anisotropic parameters for corresponding atoms constrained to be equal as far as allowed by symmetry.

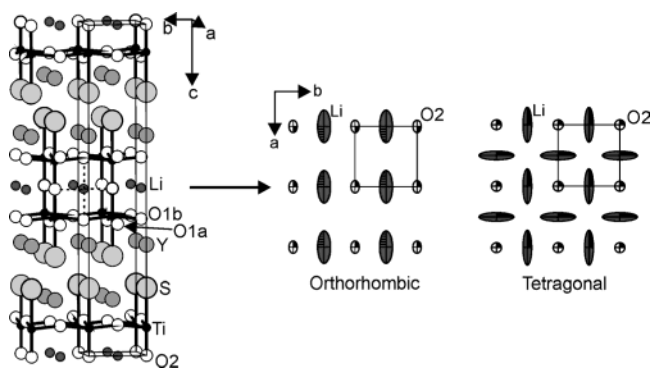**Figure 4.** Structure of orthorhombic $Li_{0.99(5)}Y_2Ti_2O_5S_2$ showing the intercalation of Li into the vacant sites within the oxide layers. The four Li–O bonding distances are indicated by dotted lines in the left-hand part of the figure. The other parts of the figure show views, down the long axis, of the Li_xO ($0 < x < 2$) sheets showing anisotropic displacement ellipsoids (99% level) in $Li_{0.99(5)}Y_2Ti_2O_5S_2$ (center) and tetragonal $Li_{1.52(5)}Y_2Ti_2O_5S_2$ (right).
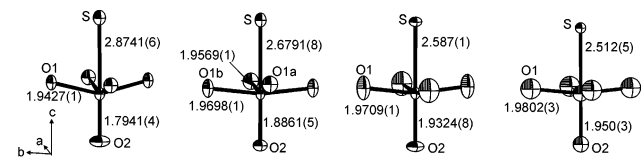
Figure 5. TiO_5S coordination polyhedra in, from left to right, $Y_2Ti_2O_5S_2$,[21] $Li_{0.99(5)}Y_2Ti_2O_5S_2$ (orthorhombic), $Li_{1.52(5)}Y_2Ti_2O_5S_2$, and $Li_{1.85(5)}Y_2Ti_2O_5S_2$. Displacement ellipsoids obtained from refinements at room temperature are shown at the 99% level (isotropic ellipsoids were used for $Li_{1.85(5)}Y_2Ti_2O_5S_2$). Bond lengths are given in angstroms.

approximately monotonically with electron count as shown in Figure 2. The long Ti–S bond shortens dramatically to 2.512(5) Å in $Li_{1.85(5)}Y_2Ti_2O_5S_2$ (Figure 6); this and the response of the YS rock salt layers to the increase in the basal dimensions lead to an approximately monotonic decrease in the c lattice parameter with electron count (Figure 2) despite the increase in the Ti–O2 bond length. The cell volume increases approximately linearly with electron count as shown in Figure 2. The changes in lattice parameters and bond lengths are approximately linear with x for the single-phase samples, and the corresponding values for lattice parameters and bond lengths derived from the refinements for the two phase sample $Li_{0.66(5)}Y_2Ti_2O_5S_2$, which we have investigated in detail, suggest

a rather narrower phase gap ($0.6 < x < 0.8$) than that suggested by the refined lithium contents of the two phases ($0.5 < x < 1$).

Physical Property Measurements. The magnetic susceptibilities of the materials measured on POLARIS are shown as functions of temperature in Figure 9. The major contribution to the susceptibility in each case is a temperature-independent term suggesting that the materials behave as Pauli paramagnets, and the electrons are largely delocalized. Small Curie contributions are consistent with around $1-3\%$ of the reduced Ti^{3+} species behaving as isolated $S = ^1/_2$ moments. The only exception to this is the least reduced compound, $Li_{0.30(5)}Y_2Ti_2O_5S_2$, in which the Curie contribution is much more important than in the other compounds and corresponds to 26% of the added electrons behaving as isolated $S = ^1/_2$ moments. Resistivity measurements performed by cold-pressing 5-mm diameter pellets (1 mm thick) at 0.5 GPa produced values of 760, 50, and 18 Ωcm for the samples $Li_{0.30(5)}Y_2Ti_2O_5S_2$, $Li_{0.99(5)}Y_2Ti_2O_5S_2$, and $Li_{1.52(5)}Y_2Ti_2O_5S_2$, respectively. The resistivities of the two lithium-richer compositions are fairly typical for unsintered pellets of fine powders of metallic oxides, suggesting that single-phase materials with $x > 1$ are metallic, while the higher resistivity of $Li_{0.30(5)}Y_2Ti_2O_5S_2$ suggests that materials with low lithium contents are semiconducting. This is consistent with the magnetic measurements, the colors of the compounds (Table 1), and the changes in structural features with x as described below. The increase in Pauli susceptibility with increasing x in $Li_xY_2Ti_2O_5S_2$ (Figure 9) indicates a proportional increase in the density of states at the Fermi level as the Ti–O antibonding bands are filled, in line with the calculations described below.

Band Structure Calculations and Interpretation of Structural Changes. To rationalize the tetragonal-to-orthorhombic-to-tetragonal structural changes as a function of x in $Li_xY_2Ti_2O_5S_2$, extended Hückel calculations were performed using the YaEHMOP[34] software package with the parameters listed in Table 6. The three-dimensional band structure and the corresponding density of states (DOS) diagram for the material with the highest experimentally attained Li content, $Li_{1.85(5)}Y_2$-

(34) Yet Another Extended Hückel Molecular Orbital Package (YAEHMOP) Home Page; Cornell University: Ithaca, NY, 1997. http://yaehmop.source-forge.net/.
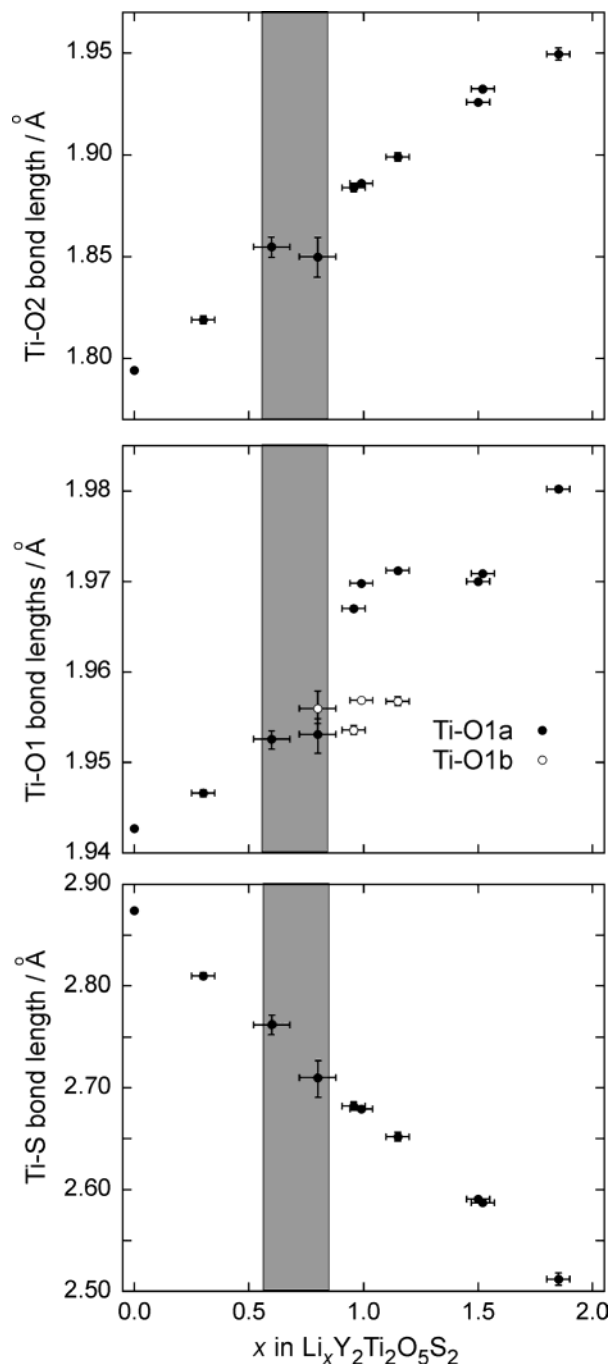
Figure 6. Axial Ti−O2 bond lengths (top), equatorial Ti−O1 (Ti−O1a (●) and Ti−O1b (○) for the orthorhombic phases) bond lengths (middle), and the Ti−S bond lengths (bottom) as functions of x for intercalates $Li_xY_2Ti_2O_5S_2$. The shaded area indicates the two-phase region.

Figure 7. Li−O1 (○), Li−O2 (●), and mean Li−O (□) distances as functions of x for intercalates $Li_xY_2Ti_2O_5S_2$. The shaded area indicates the two-phase region. The lines are guides to the eye.

Figure 8. O−Ti−O angles as functions of x for intercalates Li_xY_2-$Ti_2O_5S_2$: O2−Ti−O1 (or O2−Ti−O1b) (●), O2−Ti−O1a (○), and O1−Ti−O1 (or O1a-Ti−O1b) (□). The shaded area indicates the two-phase region.

$Ti_2O_5S_2$, are presented in Figure 10. The valence states of O and S are fully occupied, corresponding to formally completed octets, and there is considerable mixing (∼30%) of Ti states below the Fermi energy as depicted in Figure 10, indicating significant covalent character in the Ti−O and Ti−S bonds. The bands at and slightly above the Fermi level are mainly Ti 3d in character with a non-negligible admixture of O 2p and S 3p states. These crystal orbitals belong to the antibonding π^*(Ti−O, Ti−S) manifold. The high energy states of Y and Li remain unoccupied, corresponding to their full valence ionization. Calculations on the unintercalated $Y_2Ti_2O_5S_2$ host yield fully occupied S 3p states and empty Ti 3d bands corresponding
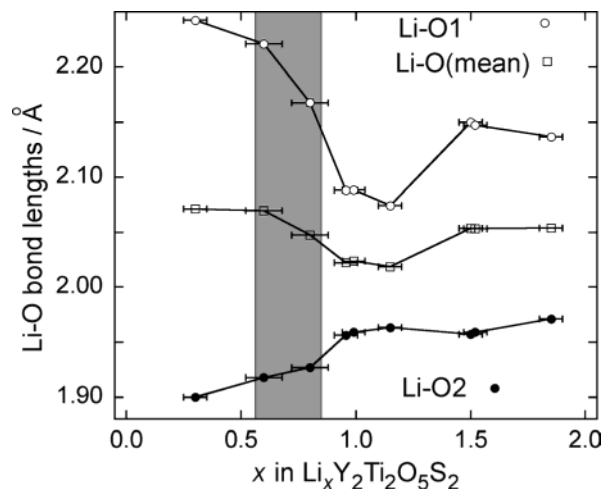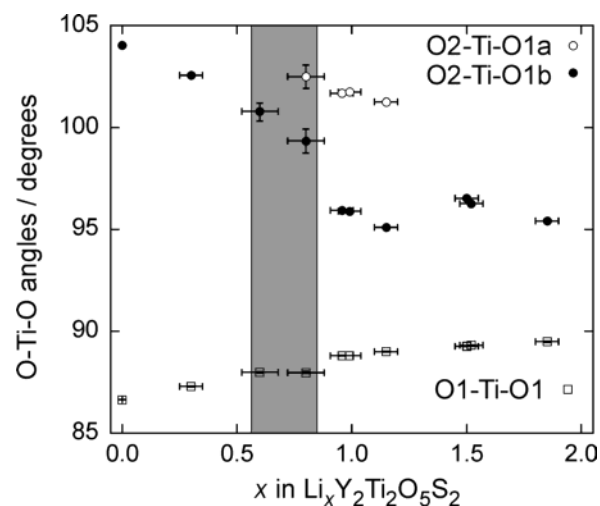
to the formal Ti^{4+} assignment and semiconducting behavior observed for the undoped material.[35] On topotactic intercalation of Li, electrons fill the lowest available Ti 3d-based bands near −9 eV. The bands are almost dispersionless along $\Gamma \rightarrow Z$ and $X \rightarrow P$, consistent with electronic isolation of the oxide slabs along the crystallographic c axis perpendicular to the layers. Thus, analysis of a single, two-dimensional $Ti_2O_{8/2}OS_2$ slab can be employed without losing any relevant features present in three dimensions. To follow the changes associated with increasing levels of intercalation in detail, the orbital contributions of the bands near the Fermi level need to be examined. Molecular orbital calculations on isolated, hypothetical TiO_5S units with the experimentally observed geometries show that the distribution of the Ti 3d orbitals closely resembles the familiar t_{2g}-below-e_g sets derived from an octahedral crystal field. Since the titanium coordination environment is distorted from O_h symmetry by replacement of one apical oxygen by sulfur, the degeneracy of the "t_{2g}" orbitals, which are first to be populated in the course of intercalation, is lifted. For all experimentally

(35) Ishikawa, A.; Takata, T.; Kondo, J. N.; Hara, M.; Kobayashi, H.; Domen, K. *J. Am. Chem. Soc.* **2002**, *124*, 13542.
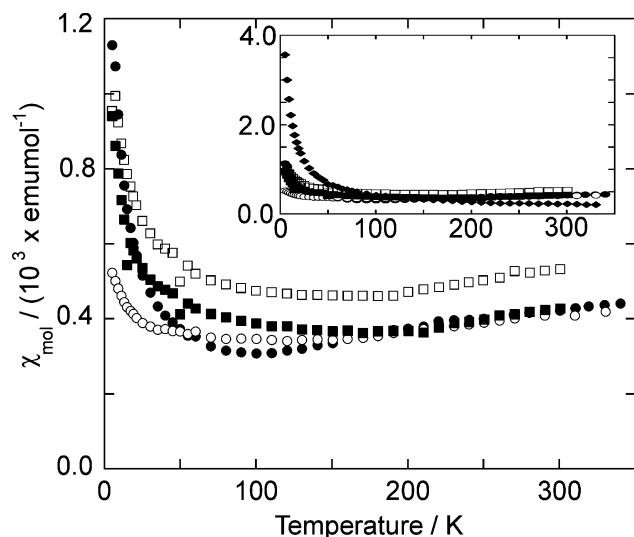
Figure 9. Magnetic susceptibilities as functions of temperature for $Li_{0.66(5)}Y_2Ti_2O_5S_2$ (two-phase mixture) (●), $Li_{0.99(5)}Y_2Ti_2O_5S_2$ (○), $Li_{1.52(5)}Y_2$-$Ti_2O_5S_2$ (■), and $Li_{1.85(5)}Y_2Ti_2O_5S_2$ (□). The inset additionally shows the larger Curie tail arising from $Li_{0.30(5)}Y_2Ti_2O_5S_2$ (◆).

Table 6. Orbital Parameters Used in Extended Hückel Calculations

atom	orbital	H_{ii} (eV)	ζ_{i1}	c_1	ζ_{i2}	c_2
Ti	4s	−8.97	1.0750			
	4p	−5.44	1.0750			
	3d	−10.81	4.55	0.4206	1.40	0.7839
O	2s	−32.30	2.2750			
	2p	−14.80	2.2750			
S	3s	−20.00	2.1220			
	3p	−11.00	1.8270			
Y	5s	−5.3370	1.2790			
	5p	−3.5150	1.0790			
	4d	−6.7990	2.5540	0.6020	1.0680	0.5780
Li	2s	−5.3420	1.0750			
	2p	−3.4990	1.0750			

determined geometries in the $Li_xY_2Ti_2O_5S_2$ series, the d_{xy} orbital is slightly lower in energy than the $d_{xz,yz}$ orbital set, which becomes nondegenerate in the orthorhombic structures with the d_{yz} orbitals being slightly more stabilized. This is illustrated for three $Li_xY_2Ti_2O_5S_2$ compositions on the sides of the three panels of Figure 11a. Joining two hypothetical TiO_5S units at their O apex, to reflect the double layer present in $Y_2Ti_2O_5S_2$ and its derivatives, allows the d orbitals to mix further with their appropriate symmetry counterpart, thus giving rise to a total of six states, which are reflected in the centers of the three panels of Figure 11a. The ± combinations of d_{xy} orbitals are separated by a small energy gap (∼0.1 eV), since their overlap is delta type and thus no orbitals at their joint oxygen apex could further participate in their mixing. The $d_{xz,yz}$ orbitals, however, mix with each other in a π fashion which also involve the $p_{x,y}$ orbitals of the apical oxygen (O2), which amounts to a larger (0.5 eV) energy difference. The antibonding (in-phase, (+)) $d_{xz,yz}$ combinations will be more stabilized than the $d_{zx,yx} - d_{xz,yz}$ bonding pair, since the in-phase (+) combination precludes mixing with the apical oxygen's orbitals, while the out-of-phase (−) combinations allow for the inclusion of O2 $2p_{x,y}$ orbitals. The molecular models help in interpreting the outcome of the two-dimensional calculations, but an additional feature needs to be accounted for in going from a molecular orbital to an extended crystal orbital system: the d_{xy} orbitals have twice as many

oxygen neighbors in the *ab* plane compared with that in the $d_{xz,yz}$ orbitals, and hence, the corresponding bandwidth of the d_{xy}-based crystal orbital is expected to be roughly twice as large as that of the $d_{xz,yz}$ bands. This unequal dispersion of the bands based on the "t_{2g}" orbitals will change the orbital order suggested by the molecular picture in Figure 11a and results in the d_{xy} states being lowest in energy at the Γ point for all geometries of intercalation. The interpretation of the band structures presented in Figure 11b follows from the above considerations. The six bands shown in each diagram contain a majority of their contributions from the six Ti 3d states derived from the hypothetical $Ti_2O_{8/2}OS_2$ molecular units. Following the arguments above, the $\pm d_{xy}$ bands follow each other closely while the $\pm d_{xz,yz}$ band centers are separated by ∼0.5 eV, and the dispersion of the d_{xy} bands is greater than that of the $d_{xz,yz}$ bands. As a consequence, the bands to be first occupied are the $\pm d_{xy}$ combinations, which can interact with the equatorial O1 $2p_{x,y}$ orbitals in a π^* fashion (for the orthorhombic cases, these equatorial oxygen atoms are designated O1a and O1b). However, due to translational symmetry requirements at Γ, no oxygen orbital is allowed to mix with the d_{xy} orbitals at this reciprocal lattice point, and the oxygen orbital contribution to the band remains quite small in going from $\Gamma \rightarrow X,Y$. This is shown in the DOS diagram presented in Figure 11c, where the orbital contribution due purely to d_{xy} states follows the total DOS very closely at low levels of lithium insertion (small x). While the d_{xy} orbital occupation increases by 7% from 0.323 in $Y_2Ti_2O_5S_2$ to 0.465 in $Li_{0.30(5)}Y_2Ti_2O_5S_2$, the Ti−O equatorial COOP values (Table 7) show very little weakening reflected in a very small increase in the corresponding bond lengths (1.9427(1) Å in $Y_2Ti_2O_5S_2$ and 1.9466(4) Å in $Li_{0.30(5)}Y_2Ti_2O_5S_2$). The integrated COOP curves in Figure 11d show that the Ti−O apical bonds are strongest, while the Ti−O equatorial bonds are slightly weaker, with the Ti−S apical bonds being weaker still. Low levels of intercalation have little influence on these bonds, and the inserted electrons will mostly occupy Ti $3d_{xy}$ states (Table 8), diminishing the already almost negligible Ti−Ti δ-bonding states listed at the bottom of Table 7. Due to the very small admixture of O $2p_{x,y}$ at small values of x, the added electrons are expected to be significantly localized in Ti $3d_{xy}$ states, and this may explain the high levels of localized magnetic moments observed in the case of $Li_{0.30(5)}Y_2Ti_2O_5S_2$ (see above).

As x in $Li_xY_2Ti_2O_5S_2$ approaches 0.7, the Fermi level reaches the base of the $d_{xz,yz}$ bands. Structures having slightly greater levels of Li intercalated show the orthorhombic distortion of the crystal structure. The largest difference in the *a* and *b* lattice parameters ($b - a = 0.09$ Å) occurs near the composition $Li_{0.99(5)}Y_2Ti_2O_5S_2$, calculations for which are presented in the middle panels of Figure 11. The lowering of symmetry removes the degeneracy of the d_{xz} and d_{yz} states, and two geometrical parameters have great influence on the nature of these bands: the different Ti−O1a and Ti−Ob bond lengths (Figure 6, Table 7) and the O2−Ti−O1a and O2−Ti−O1b angles (Figure 8), which reflect the departure of the oxygen atoms from the plane described by the Ti atoms. The Ti−O1b bond length is only slightly longer (0.01 Å) than the Ti−O1a distance. Much more noticeable (Figure 8) is the 5.8° difference between the O2−Ti−O1a (101.74(2)°) and O2−Ti−O1b (95.90(2)°) angles: the O1b atoms located along the *b*-axis (the longer axis) lie much closer to the plane described by the Ti atoms than the O1a atoms
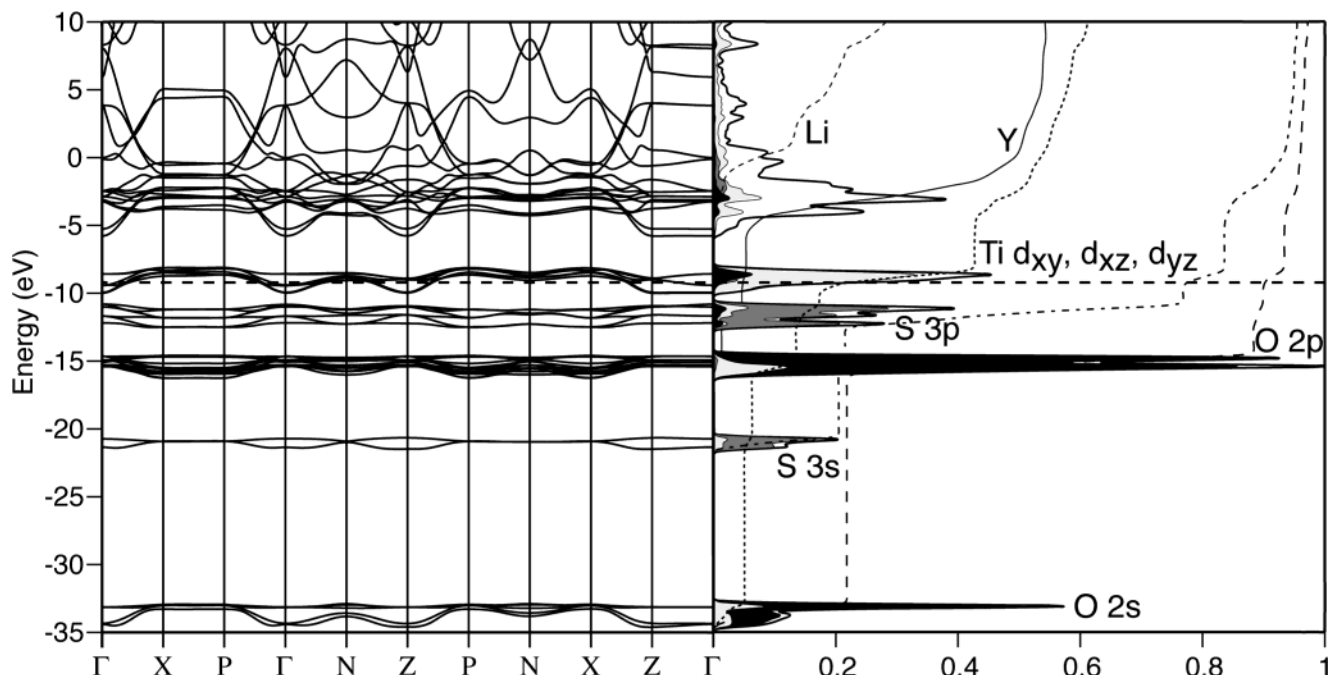
Figure 10. Band structure (left) and DOS (right) for $Li_{1.85(5)}Y_2Ti_2O_5S_2$. The Fermi energy is indicated by the dashed horizontal line at -9 eV. The black projected DOS insets show the distribution of oxygen-based orbitals, while the medium and light gray areas show S and Ti orbital contributions, respectively. Dashed lines indicate integrated occupation of atomic states.

along the *a*-axis (the shorter axis), as shown in Figure 5. The energetic stabilization of the d_{yz} states over the d_{xz} states depicted in Figure 11c is a direct consequence of this change in geometry between the tetragonal and orthorhombic symmetries. Translational symmetry requirements mean that at Γ, the $d_{xz,yz}$ orbitals are unable to engage in any bonding with the O1a or O1b $2p_z$ orbitals, irrespective of the level of out-of-plane bending. The $O1a$-$2p_x$/$O1b$-$2p_y$ orbitals do, however, have nonzero overlap with Ti $d_{xz,yz}$ orbitals because the O1a/O1b atoms lie out of the plane of the Ti atoms. Near the Fermi energy, the mixing between these orbitals will be antibonding. Because the O1-$2p_x$/p_y–Ti-$3d_{xz}$/d_{yz} mixing vanishes when the oxygen and titanium atoms lie in the same plane, the closer the oxygen atoms are to the plane of Ti atoms, the less will be the destabilization of the corresponding Ti 3d-based crystal orbital. The O1b atoms approach the Ti plane more closely than the O1a atoms do; thus, the d_{yz} orbitals lie lower in energy than the d_{xz} orbitals, as shown in Figure 11, parts a–c. The orbital occupation of the d_{yz} states increases from 0.362 to 0.527 on going from $x = 0.30(5)$ to $x = 0.99(5)$, while the orbital occupation of the higher-energy d_{xz} orbitals remains almost unchanged (0.362 in $Li_{0.30(5)}Y_2Ti_2O_5S_2$ and 0.372 in $Li_{0.99(5)}Y_2Ti_2O_5S_2$). However, the integrated COOP values show negligible contrast between the Ti–O1a and Ti–O1b bonding (0.489 and 0.488, respectively, at $x = 0.99(5)$), and both bonds are only slightly weaker than at lower levels of intercalation (0.497 at $x = 0.30(5)$). The retention of the Ti–O1b bond strength is possible since the proportion of O1b-$2p_y$ orbitals present below -9 eV in the d_{yz} crystal orbital is still very small. The orthorhombic distortion allows the accommodation of additional electrons with only a slight decrease in the Ti–O1b bond strength since the distortion is such that the occupied $3d_{yz}$ orbitals become less antibonding. The Ti–O1a bonds remain strong and short as possible since the distortion allows occupancy of the $3d_{xz}$ antibonding orbitals to be avoided.

For $x \geq 1.5$, the structure returns to tetragonal symmetry. The results presented on the right-hand panels of Figure 11 correspond to the structure of $Li_{1.85(5)}Y_2Ti_2O_5S_2$, where the $3d_{xz}$ and $3d_{yz}$ states are again constrained to be degenerate by symmetry. There is a further increase in the atomic occupation of these orbitals accompanied by a much larger reduction in their COOP values (from 0.489 in $Li_{0.99(5)}Y_2Ti_2O_5S_2$ to 0.468 in $Li_{1.85(5)}Y_2Ti_2O_5S_2$), signaling the onset of weakening in Ti–O1 π-bonding. Our calculations cannot reliably predict the minimum level of intercalation necessary to initiate the orthorhombic-to-tetragonal transition (which must lie in the range $1.3 < x < 1.5$), but the results show that there is a limited amount of electron filling where the distortion to orthorhombic symmetry allows the antibonding d_{xz} bands to remain unoccupied; at greater electron counts, the incentive for the above-described distortion vanishes.

The decrease toward 90° of the O2–Ti–O1 angles with increasing x (Figure 8), decreases the antibonding nature of the $3d_{xz}$ and $3d_{yz}$ orbitals. Any decrease in the bond strength of the Ti–O framework is compensated by an increase in Ti–S bonding. Indeed, the most substantial structural change during the course of intercalation occurs in the Ti–S distance (Figure 6), which decreases from 2.8741(6) Å in $Y_2Ti_2O_5S_2$[21] to 2.512(5) Å in $Li_{1.85(5)}Y_2Ti_2O_5S_2$. The shortest distance is comparable to the bond lengths observed in related titanium sulfides ($LiTiS_2$ 2.481 Å; $Li_{0.33}TiS_2$ 2.509 Å)[36] and indicates a full-fledged Ti–S bond. The COOP curves in Figure 11d show the progression of increased Ti–S bonding with increasing Li content. For $x > 1$, the Ti–S bond strength apparently exceeds that of any Ti–O interaction, doubling in value between $x = 0$ and $x = 1.85(5)$. At $x = 1.85(5)$, the Ti–S bond has reached its maximum potential, and further electrons entering the conduction bands

(36) (a) Patel, S. N.; Balchin, A. A. *Z. Kristallogr.* **1983**, *164*, 273. (b) Dahn, J. R.; McKinnon, W. R.; Haering, R. R.; Buyers, W. J. L.; Powell, B. M. *Can. J. Phys.* **1980**, *58*, 207.
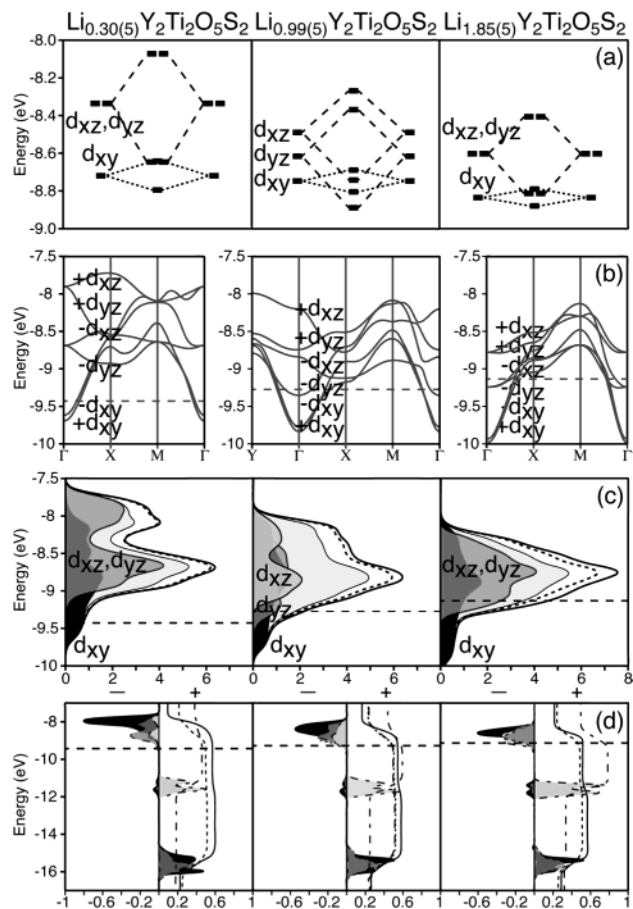
Figure 11. (a) Molecular orbital picture for the Ti 3d-derived orbitals of a fragment obtained by joining two TiO_5S octahedra at a common oxide vertex using geometries obtained by Rietveld refinement against neutron data for $Li_xY_2Ti_2O_5S_2$ $x = 0.30(5)$ (left), tetragonal; 0.99(5) (center), orthorhombic; and 1.85(5) (right), tetragonal. Extension to the two-dimensional $Ti_2O_5S_2$ slabs produces the Band structures (b), DOS (c) and COOP curves (d) for the three compositions. In (c), the individual and total Ti 3d contributions to the DOS are indicated as shaded regions; the dashed lines incorporate oxygen states, and the outer solid line is the total DOS incorporating the sulfur states. In (d), the COOP curves for Ti−O2 apical (dark-shaded/solid line), Ti−O1 equatorial (medium-shaded/short-dashed line), and Ti−S (light-shaded/long-dashed line) are shown with corresponding integrated curves.

would begin to occupy Ti−S π^* antibonding states. Thus, the $Y_2Ti_2O_5S_2$ host can accommodate close to one Li per Ti without losing much in the overall cohesion by a gradual decrease in the Ti−S distance, which has a very limited influence in the Ti−O framework in the *ab* plane.

Thus, the degree of orthorhombic distortion also increases with electron count to maintain the edge of the unfilled $3d_{xz}$ above the Fermi energy. In a solid-state system, the extent of such a distortion is constrained by the other parts of the structure, so at high electron counts, corresponding to high levels of Li intercalation, partial filling of the $3d_{xz}$ band is unavoidable. The transition to orthorhombic symmetry is electronically driven by lifting the degeneracy of the Ti $3d_{xz}$ and $3d_{yz}$ and occurs with retention of the unit cell (aside from the slight increase in volume). It should thus be understood as analogous to a cooperative Jahn−Teller type distortion.

In the orthorhombic compound $Li_{0.99(5)}Y_2Ti_2O_5S_2$, measured on POLARIS as well as those with similar compositions measured on D2B, lithium occupies only one of the two available four-coordinate planar sites in the perovskite blocks,

as shown in Figure 4. The Li−O bond lengths are shown as a function of *x* in Figure 7. Although the Lib−O2 distance, corresponding to half of the *b*-axis length, is slightly longer (1.95941(2) Å) than the corresponding distance for occupation of the Lia site (1.913 Å), the decrease in the O2−Ti−O1b angle (95.90(2)°) relative to the O2−Ti−O1a angle (101.74(2)°), described above, makes the axial O1b−Lib contact much shorter (2.0884(4) Å) than the O1a−Lia alternative (2.281 Å). Thus, the electronically driven orthorhombic distortion is reinforced by providing more favorable electrostatic Li−O cohesion. Increasing the lithium content above 1.0 must entail partial filling of the Lia site, although we have not investigated this in detail.

Interpretation of Phase Gap Behavior. At the compositions close to the change from tetragonal to orthorhombic symmetry ($x \approx 0.7$), there is a phase gap with coexistence of a tetragonal phase and a Li-richer orthorhombic phase. This is good evidence that the change from tetragonal to orthorhombic symmetry is electronically driven rather than merely driven by the coordination preferences of Li^+. Presumably the two phases identified as representing the edges of the phase gap have similar chemical potentials, which are both lower than that of a hypothetical single tetragonal phase with the chemical composition of the sample. At elevated temperatures (above 200 °C), a single tetragonal phase *does* exist, and our variable temperature PND study shows that this disproportionation is reversible. This transformation requires that the lithium ion has a high mobility below 200 °C. The two phases present at room temperature in the sample $Li_{0.66(5)}Y_2Ti_2O_5S_2$ have very similar unit cell volumes despite their different lithium contents (Figure 2). Since their lattice parameters were measured in a single experiment this must reflect a true departure from the general trend in increasing cell volume with electron count (Figure 2). The Ti−O bond lengths in the two-phase region also depart from the general trends (Figure 6); the closely similar mean Ti−O bond lengths in the two-phase region of 1.933(2) Å and 1.934(2) Å for the tetragonal and orthorhombic phases, respectively, should be compared with the linear 3% increase in the mean Ti−O distance from 1.913(1) Å in $Y_2Ti_2O_5S_2$[21] to 1.974(1) Å in $Li_{1.85(5)}Y_2Ti_2O_5S_2$. These observations are consistent with a transition from localized to itinerant electron behavior with increasing *x*, separated by the two-phase region, with the Li-richer metallic phase having a smaller cell volume and shorter mean Ti−O distance than expected for an imaginary isoelectronic insulating phase.[37] Coincidence of the insulator to metal transition with the tetragonal to orthorhombic distortion is also consistent with the electrical resistivity and magnetic susceptibility measurements described above and with the colors of the materials. In the analogous sodium intercalates[21] in which Na^+ is located in the 12-coordinate site, the cooperative distortion observed here does not occur, rather local lifting of the C_{4v} symmetry is manifested as crystallographic disorder in the equatorial oxygen positions (i.e., O1), as described elsewhere.[21]

Comparison with Other Lithium Intercalates. The structures of the analogous lithium intercalates of WO_3 and ReO_3 have been established previously.[38−40] In the former case,

(37) Goodenough, J. B. *Struct. Bonding (Berlin)* **2001**, *98*, 1.
(38) Wiseman, P. J.; Dickens, P. G. *J. Solid State Chem.* **1976**, *17*, 91.
(39) Cava, R. J.; Santoro, A.; Murphy, D. W.; Zahurak, S.; Roth, R. S. *J. Solid State Chem.* **1982**, *42*, 251.
(40) Cava, R. J.; Santoro, A.; Murphy, D. W.; Zahurak, S.; Roth, R. S. *J. Solid State Chem.* **1983**, *50*, 121.

Table 7. Average Values of Crystal Orbital Overlap Populations (COOPs) and Bond Lengths (Å) for $Li_xY_2Ti_2O_5S_2$

bond	$x = 0$	$x = 0.30$	$x = 0.99$	$x = 1.85$
Ti−O2 (apical)	0.588	0.570	0.546	0.516
	$(1.7941(4))^a$	(1.819(2))	(1.8861(5))	(1.950(3))
Ti−O1a (equatorial)	0.500	0.497	0.489	0.468
	$(1.9427(1))^a$	(1.9466(4))	(1.9569(1))	(1.9801(3))
Ti−O1b (equatorial)	0.500	0.497	0.488	0.468
			(1.9698(1))	
Ti−S (apical)	0.407	0.457	0.581	0.748
	$(2.8741(6))^a$	(2.810(3))	(2.6791(8))	(2.512(5))
Y−S	0.258	0.250	0.225	0.193
	$(2.8048(2))^a$	(2.823(1))	(2.8781(2))	(2.920(1))
Ti−Ti (along a)	0.021	0.007	−0.001	−0.016
	$(3.76956(1))^a$	(3.80002(2))	(3.83189(3))	(3.94260(8))
Ti−Ti (along b)	0.021	0.007	−0.010	−0.016
			(3.91881(3))	
Ti−Ti (along c)	0.024	0.018	0.003	−0.011
	$(3.588(1))^a$	(3.638(3))	(3.768(1))	(3.888(4))

a Results from ref 21.

Table 8. Atomic Orbital Occupations Derived from Extended Hückel Calculations

Ti orbital	$x = 0$	$x = 0.3$	$x = 0.99$	$x = 1.85$
$3d_{xy}$	0.323	0.465	0.649	0.819
$3d_{xz}$	0.356	0.362	0.372	0.592
$3d_{yz}$	0.356	0.362	0.520	0.592
$3d_{z^2}$	0.459	0.469	0.490	0.511
$3d_{x^2-y^2}$	0.374	0.375	0.377	0.376

intercalation up to $Li_{0.36}WO_3$[38,40] results in distortion of the WO_3 framework and accommodation of lithium in a four-coordinate square planar site. This site is in the center of the 12-coordinate vacant cation site in WO_3, and the tilting distortion of the WO_6 octahedra is such that four of the oxide anions surrounding the vacancy move toward the original 12-coordinate site and coordinate to Li (Li−O distances: 2.192(2) Å × 4). Similar behavior is observed in $Li_{0.2}ReO_3$.[40] The 4-coordinate site occupied in the $Li_xY_2Ti_2O_5S_2$ intercalates lies, in contrast, *between* two 12-coordinate vacancies, and the mean Li−O bond lengths (Figure 7) are rather shorter than those in the WO_3 and ReO_3 intercalates but are similar to the sum of the Li^+ and O^{2-} radii. In $Li_2FeV_3O_8$,[41] the Li intercalate of FeV_3O_8, Li occupies an approximately square pyramidal site with a mean Li−O distance of 2.04(3) Å. In the Li-rich intercalates of ReO_3 ($LiReO_3$ and Li_2ReO_3),[39] there are very significant tilting distortions of ReO_6 octahedra which result in each 12-coordinate vacant cation site transforming to a pair of face-shared octahedral sites which are all filled in Li_2ReO_3. Li is displaced from the centers of these octahedral sites (Li−O distances of 1.95(1) × 3 and 2.30(2) × 3). The coordination environment observed in the $Li_xLn_2Ti_2O_5S_2$ intercalates is thus comparable

in terms of geometry, coordination number, and Li−O separations with that observed in other Li-intercalated oxides. The distortions displayed by the Li-poor and Li-rich intercalates of WO_3 and ReO_3 are a response to the coordination preferences of Li^+ and are available on account of the fact that the WO_6 and ReO_6 octahedra share vertices only, allowing distortion by relative tilting of the octahedra. Although the TiO_5S polyhedra in $Ln_2Ti_2O_5S_2$ share vertices, the layered nature of the structure and the restraining presence of the YS "rock salt" layers precludes such distortions.

Conclusion

The $Li_xLn_2Ti_2O_5S_2$ compounds offer an unusual example of a series in which the rigidity of the two-dimensional framework and the relatively low steric demands of the lithium ion permit the electronic effects of intercalation to dominate the details of the structure. The system shows qualitative similarities to the $La_{1-x}Sr_xTiO_3$ perovskite system[26,37] in which a metal-to-insulator transition occurs across the two-phase region $0.05 \leq x \leq 0.08$ and is complementary to other two-dimensional reduced titanates such as the $NaTiO_2$ system[27] in which an electronically driven structural distortion is evident in a system containing layers of edge-sharing TiO_6 octahedra.

(41) Cava, R. J.; Santoro, A.; Murphy, D. W.; Zahurak, S.; Roth, R. S. *J. Solid State Chem.* **1983**, *48*, 309.